



The intercalation chemistry of $\text{H}_2\text{V}_3\text{O}_8$ nanobelts synthesised by a green, fast and cost-effective procedure

Jesús Prado-Gonjal^a, Beatriz Molero-Sánchez^a, David Ávila-Brandé^a, Emilio Morán^a, Juan Carlos Pérez-Flores^b, Alois Kuhn^b, Flaviano García-Alvarado^{b,*}

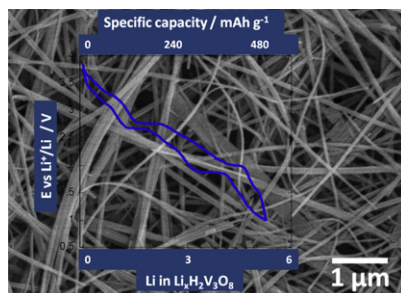
^a Universidad Complutense de Madrid, Facultad de Ciencias Químicas, Departamento de Química Inorgánica, 28040 Madrid, Spain

^b Universidad CEU San Pablo, Facultad de Farmacia, Departamento de Química, Urbanización Montepríncipe, 28668 Boadilla del Monte, Madrid, Spain

HIGHLIGHTS

- ▶ $\text{H}_2\text{V}_3\text{O}_8$ nanobelts synthesised in just 2 h.
- ▶ Electrochemical properties of as prepared $\text{H}_2\text{V}_3\text{O}_8$ similar to samples prepared by more expensive routes.
- ▶ EELS experiments show full reduction to V^{3+} .
- ▶ Extra capacity can be obtained down to 1 V but of little practical use.
- ▶ Remarkable stability of a protonated compound upon intercalation.

GRAPHICAL ABSTRACT



ARTICLE INFO

Article history:

Received 23 October 2012

Received in revised form

15 December 2012

Accepted 27 December 2012

Available online 12 January 2013

Keywords:

Lithium batteries

Green chemistry

Microwave-assisted hydrothermal synthesis

Lithium intercalation

EELS

ABSTRACT

$\text{H}_2\text{V}_3\text{O}_8$ nanobelts have been successfully synthesised from commercial V_2O_5 powder through a fast and environmental friendly microwave-hydrothermal method. X-ray diffraction, field-emission scanning electron microscopy, thermogravimetric analysis, infrared spectroscopy, high-resolution transmission electron microscopy and ICP spectroscopy were used to characterise the morphology and structure–microstructure details. Nanobelts about 100 nm wide and several micrometres long are easily prepared in no more than 2 h. The electrochemical study reveals the reversible insertion of ca. 4 Li per formula unit (400 mAh g^{-1}), through several pseudo-plateaus in the 3.75–1.5 V vs Li^+/Li voltage range showing the interest of this material produced by a “green” route as an electrode for lithium rechargeable batteries. After the first cycle a significant capacity loss is observed, though a high capacity, ca. 300 mAh g^{-1} , remains upon cycling. Furthermore, the similarity of discharge and charge curves, pointing to the absence of hydrogen displacement during lithium insertion in $\text{H}_2\text{V}_3\text{O}_8$, shows that not all protonated systems must be discarded as prospective electrode materials.

On the other hand, further reduction down to 1 V is possible to insert up to 5 Li per formula unit (480 mAh g^{-1}). Interestingly it corresponds to full reduction of vanadium to V^{3+} as it is also confirmed by EELS experiments. However, the full reduction to V^{3+} is associated with a fast decay of the extra capacity developed at low voltage with increasing current rate. Then for practical use we may consider only the capacity obtained down to 1.5 V.

© 2013 Elsevier B.V. All rights reserved.

1. Introduction

Vanadium oxides, oxyhydroxides and hydrated oxides with one-dimensional (1D) nanostructures, such as nanobelts, nanoribbons or nanorods, have attracted great attention due to their diverse

* Corresponding author. Tel.: +34 91 3724 728; fax: +34 91 3510496.

E-mail addresses: flaga@ceu.es, flaviano.garcia@hotmail.com (F. García-Alvarado).

physicochemical properties. These oxides present a large number of different structures and exist in a range of single and mixed metal oxidation states (from +2 to +5) [1]. They are excellent electrode materials for rechargeable lithium batteries, due to their large specific capacity, good cyclability and low cost as well.

Controlling the growth, size and shape of nanosized objects are important research areas in materials science. In fact, the physical properties depend not only on the composition but also on the particle size and shape. The electrochemical behaviour of these materials strongly depends on these factors and usually, the smaller the particle size is, the lower the cell polarization and the higher the cell capacity become [2–4].

$\text{H}_2\text{V}_3\text{O}_8$ is one of the most attractive vanadium oxide hydrates due to its interesting electrochemical properties. Early works reported the insertion of up to 2.5 Li/formula unit (Li/f.u. hereafter) in the 4–1.5 V range corresponding to a specific capacity of 240 mAh g^{-1} [1,5]. Interestingly, simultaneous oxidation and partial exchange of H by alkali metals produced superior performances. For example, $\text{Na}_{0.9}\text{H}_{0.1}\text{V}_3\text{O}_8$ inserts 2.9 Li/f.u and develops 260 mAh g^{-1} , due to the larger extent of the proton exchange and the better ordered structure [5,6].

The synthesis of this material was first reported by Théobald and Cabala using a hydrothermal treatment [7]. The crystal structure presents orthorhombic symmetry (S.G. #62 *Pham*). The structural model was first described by Oka et al. [8], as a nearly layered arrangement (V_3O_8), where two different VO_x polyhedra are present: VO_6 octahedra and VO_5 trigonal bipyramids with vanadium oxidation states of +4, +5 in the former and +5 in the latter.

The more common hydrothermal treatment implies the use of sealed Pyrex ampoules containing aqueous VOSO_4 or solutions with different reduced vanadium compounds, which are heated at 180–220 °C for several hours or up to several days [2,6,8,9]. Alternatively, it can be prepared from V_2O_5 xerogel to avoid using a precursor containing V^{4+} [10]. However, this route is energy cost ineffective inasmuch as the xerogel has to be previously prepared at high temperature, 800 °C.

Due to the technological interest of $\text{H}_2\text{V}_3\text{O}_8$, a big effort is being made in order to improve its synthesis and electrochemical performance connected to low production costs. Therefore, recent reports on the synthesis of $\text{H}_2\text{V}_3\text{O}_8$ describe the preparation from the cheapest and more available vanadium oxide, V_2O_5 [11,12].

Regarding electrochemical performances, the highest specific capacity reported up to now is 409 mAh g^{-1} corresponding to the insertion of 4.32 Li/f.u in the 4–1.5 V voltage range [9]. Interestingly, the material was prepared as single crystal nanobelts through a hydrothermal route at 180 °C for 7 days from a mixture of V_2O_3 and V_2O_5 .

In this paper we present a novel and more efficient synthesis route combining hydrothermal method with microwave irradiation. This is an effective method to produce nanoparticles as well as controlling the particle size through different mechanisms of nucleation and growth kinetics. Furthermore, the time required for the synthesis has been significantly reduced compared with the present state-of-art, from several days [2,6,9–11] to only 2 h and using environmentally friendly reagents while maintaining similar electrochemical performances. This involves much less energy compared with other hydrothermal routes reported up to day. This new synthetic procedure is consistent with most of the “Green Chemistry” principles: waste prevention, atoms economy, not dangerous synthesis using safe reactants and solvents (V_2O_5 , ethanol and water), high efficiency in terms of energy (2 h of reaction) and yield (close to 100%) and easily monitoring to prevent any kind of pollution.

When microwave irradiation is combined with hydrothermal method, an important step is the choice of solvent [13,14].

The coupling efficiency of a solvent is very important to the outcome of the reaction. The more efficient a solvent is in coupling with the microwave energy, the faster the temperature of the reaction mixture increases. There are three main dielectric parameters that are related to the ability of a solvent to absorb microwave energy: (1) tangent delta (δ) or loss tangent that is the dissipation factor of the sample or how efficiently microwave energy is converted into thermal energy, (2) dielectric loss (ϵ'') corresponding to the amount of input microwave energy that is lost by dissipation, and (3) dielectric constant (ϵ') of the solvent that is the ability to store electric charges. For example, ethanol can be categorized as a high absorber ($\epsilon' = 24.3$; $\tan \delta = 0.9$; $\epsilon'' = 22.9$, at room temperature and 2.45 GHz frequency) while water, although having the highest dielectric constant, is a medium absorber due to its moderate $\tan \delta = 0.1$ and dielectric loss values, $\epsilon' = 80.4$ and $\epsilon'' = 9.9$, respectively, at room temperature and 2.45 GHz [15,16].

We show that $\text{H}_2\text{V}_3\text{O}_8$ nanobelts are produced by microwave-hydrothermal reaction as an example of green chemistry applied to the synthesis of an electrode material. The characterisation of the prepared materials, as well as their intercalation chemistry, is presented. The study includes the evolution of vanadium oxidation state from mixed $2 \text{V}^{5+} + 1 \text{V}^{4+}$ to 3V^{3+} . High capacities, even at high current densities, have been found in this study showing that microwave-hydrothermal method is a promising synthetic procedure to prepare electrode materials in a fast and environmental friendly way; a very important aspect when assessing the scaling up to allow lithium batteries to fully attend the high demand of production in the near future electric vehicle market. Interestingly, a preprint has been made recently available describing the application of a similar procedure to the preparation of compounds of general formula $\text{VO}_x \cdot n\text{H}_2\text{O}$ with application in aqueous-based Li-ion supercapacitors [17], albeit due to the lack of structural characterisation the true nature of those $\text{VO}_x \cdot n\text{H}_2\text{O}$ was not unveiled.

2. Experimental procedure

2.1. Synthesis

A commercial Milestone ETHOS 1 apparatus operating at 2.45 GHz and equipped with a stirring motor was used. Although the same frequency is used in domestic microwave ovens, this equipment allows fully automated operation of the most important reaction parameters (pressure, power-temperature and time) [18]. The reaction was carried out in a quartz pressure vessel (45 ml with 40 bars and 250 °C as maximum pressure and temperature values, respectively). The reactants V_2O_5 (0.5 mmol, Aldrich, 98%) and ethanol (5 ml, Scharlau, synthesis grade) are mixed in 20 ml distilled water as solvent and placed and stirred in the vessel. The optimised heating program used was as follows: a heating slope to 200 °C for 15 min, then 2 h at 200 °C followed by switching off the microwave. The reaction vessel was connected to a pressure transducer in order to monitor the autogenous pressure, which was found to be around 21 bars during the whole period at 200 °C; besides, power was limited to 500 W. The as obtained product was finally washed with distilled water and dried at 80 °C. This product can be observed by eye to form an entangled green sheet.

2.2. Characterisation

An inductively coupled plasma optical emission spectrometer with axial and radial viewing plasma configuration (ICP-OES Perkin–Elmer Model Optima 3300 DV) operating at a 40 MHz free-running ratio-frequency and provided with a TRACYC44 auto sampler (Perkin–Elmer) was utilized to determine vanadium content of the sample.

Purity and structure of the sample were determined by powder X-ray diffraction (XRD) on a Bruker D8 high-resolution diffractometer, using monochromatic Cu $K_{\alpha 1}$ ($\lambda = 1.5406 \text{ \AA}$) radiation obtained with a germanium primary monochromator, and equipped with a solid-state rapid LynxEye detector. Le Bail fitting was carried out using the FullProf software [19].

The sample was sputter coated (EMITECH K550) with Au to enable field-emission scanning electron microscopy (FE-SEM) by using a JEM 6335 F electron microscope with a field-emission gun operating at 10 kV. For high-resolution transmission electron microscopy (HRTEM) a sample was prepared from $\text{H}_2\text{V}_3\text{O}_8$ powder suspended and ultrasonically dispersed in *n*-butanol. One drop of the corresponding suspension was placed on a Cu grid with holey carbon film. Experiments were performed using a JEOL 3000F with a resolution limit of 1.1 \AA . Besides, the experimental HRTEM images were simulated using MacTempas software. Electron energy loss spectroscopy (EELS) studies were performed in a Philips CM200FEG electron microscope (point resolution $\sim 0.23 \text{ nm}$, acceleration voltage of 200 kV), equipped with a Gatan Image Filter GIF200 spectrometer (energy resolution $\sim 0.70 \text{ eV}$).

An Infrared (IR) spectrum of a KBr pellet ($\sim 150 \text{ mg}$) containing approximately 2 mg of $\text{H}_2\text{V}_3\text{O}_8$ dried previously at 80°C was recorded by using an FTIR Thermo-Nicolet 200 spectrophotometer in the $4000\text{--}400 \text{ cm}^{-1}$ frequency range.

Thermogravimetric analysis (TGA) was performed on a Cahn D-200 electrobalance using H_2 (200 mbar)/He (400 mbar) atmosphere. The sample was heated at 5°C min^{-1} up to 550°C .

Specific surface area (SSA) measurements were carried out by the Brunauer, Emmett and Teller (BET) method [20]. Nitrogen adsorption–desorption isotherms and Barrett–Joyner–Halenda (BJH) pore size distribution were recorded using a Micromeritics ASAP 200 surface analyzer. Prior to measurement the powder samples were placed in a glass cell and heated in vacuum at 110°C for 180 min in order to remove the absorbed water content and other contaminants by degassing, which is essential to facilitate an accurate surface area determination. The BET analysis cell was cooled by immersion into a liquid nitrogen Dewar to get a 77 K constant temperature during the measurement. Collected data are displayed in the form of a BET isotherm, which plots the amount of gas adsorbed as a function of the relative pressure [21,22].

Electrochemical characterisation of $\text{H}_2\text{V}_3\text{O}_8$ was performed in CR2032 coin cells to investigate the lithium insertion and deinsertion reaction. A lithium foil was used as the negative electrode, while the positive electrode was obtained with the as prepared powder, dried at 80°C and manually mixed with carbon black and a binder agent (Kynarflex) in a 75:20:5 weight ratio. Pellets of 8 mm diameter and containing typically 11–14 mg of sample were conformed from this mixture by uniaxial pressing. A 1M LiPF_6 solution in EC:DMC (1:1) was used as the electrolyte (commercial battery electrolyte LP30, Selectipure™). Cells were run using a MacPile II system. Galvanostatic experiments at constant current corresponding to different C/n discharge rates (n stands for the number of hours needed to insert 1 Li/f.u.) were carried out to characterise the response of the electrode material; additionally galvanostatic experiments at $C/20$ were used to synthesise different $\text{Li}_x\text{H}_2\text{V}_3\text{O}_8$ samples in order to be characterised by EELS. Experiments close to equilibrium were carried out using the potentiostatic intermittent titration technique (PITT) at 25°C by changing the potential in intervals of $\pm 10 \text{ mV}$ every 12 h.

3. Results and discussion

The XRD pattern of the green powder obtained by microwave-hydrothermal treatment is shown in Fig. 1. Diffraction peaks can be indexed, using Le Bail fitting, to the *Pnam* (#62) orthorhombic

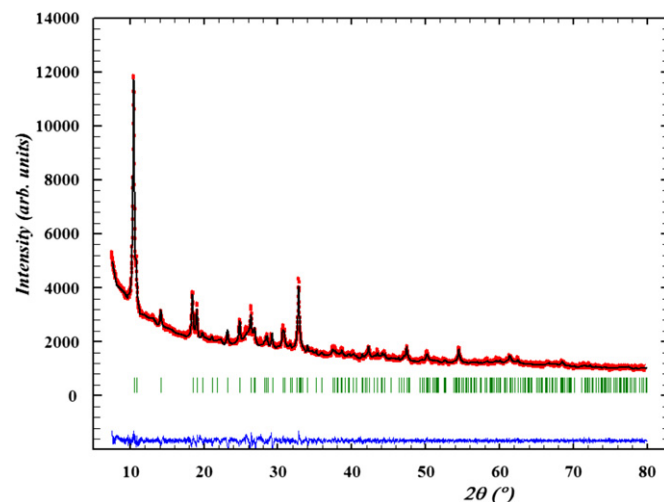


Fig. 1. Experimental (red circles) and calculated (black continuous line) XRD pattern (and their difference, blue line at the bottom) for $\text{H}_2\text{V}_3\text{O}_8$ (S.G. *Pnam*) prepared by microwave-hydrothermal route after 2 h of treatment. (For interpretation of the references to color in this figure legend, the reader is referred to the web version of this article.)

system with lattice constants $a = 16.809(2) \text{ \AA}$, $b = 9.303(1) \text{ \AA}$ and $c = 3.62444(5) \text{ \AA}$, which are similar to the values previously reported in the literature for $\text{H}_2\text{V}_3\text{O}_8$ (ICDD 04-011-3466) [7].

On the other hand, the stoichiometry of the $\text{H}_2\text{V}_3\text{O}_8$ sample was confirmed by ICP-OES. This analysis reveals vanadium contents of $51 \pm 2\%$, in quite good agreement with the theoretical value (54%).

The structure was confirmed at the local level by IR spectroscopy. Fig. 2 shows the IR spectrum of a sample heated at 80°C in order to remove absorbed water. It has been assigned as previously reported for $\text{H}_2\text{V}_3\text{O}_8$ [11,23]. The broad band at 3416 cm^{-1} comes from the OH group vibrations, together with a narrow band at 1637 cm^{-1} band which is ascribed to H_2O bending mode. Both vibrations indicate the presence of coordination water in agreement with the structure proposed by Oka et al. [8]. The bands at 1021 cm^{-1} and 975 cm^{-1} correspond to the symmetric stretching of the ($\text{V}^{5+}=\text{O}$) and ($\text{V}^{4+}=\text{O}$) bonds, respectively, showing the presence of mixed valence state vanadium.

The SEM image displayed in Fig. 3 clearly shows the morphology of $\text{H}_2\text{V}_3\text{O}_8$ nanobelts obtained using the microwave-hydrothermal route. They exhibit a width close to 100 nm and a length of several tens micrometres.

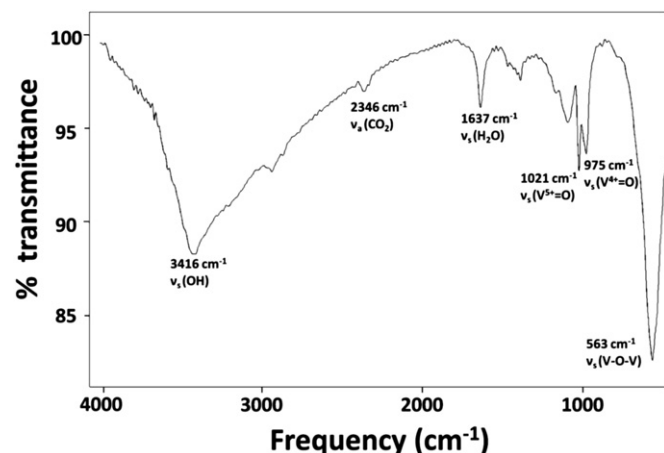


Fig. 2. FTIR spectrum of $\text{H}_2\text{V}_3\text{O}_8$ prepared by microwave-hydrothermal route.

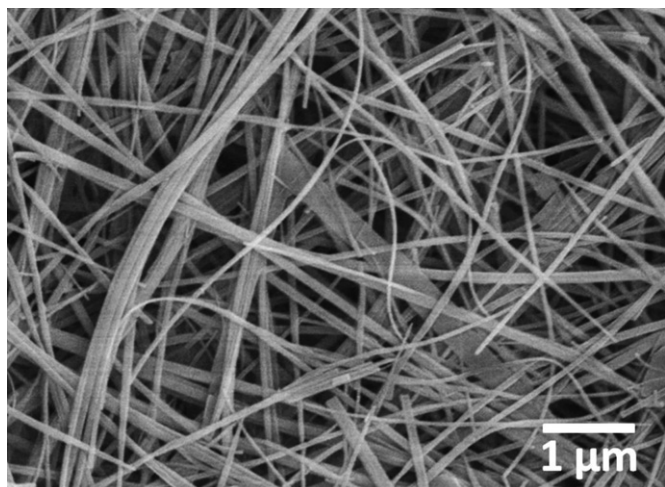


Fig. 3. Nanobelt morphology typical of $\text{H}_2\text{V}_3\text{O}_8$ prepared by microwave-hydrothermal route.

On the other hand, the analysis of the HRTEM images of the nanobelts is in full agreement with the structure proposed for $\text{H}_2\text{V}_3\text{O}_8$. A structural image along the $[100]$ zone axis (see Fig. 4a) shows a regular stacking with periodicity of 0.36 and 0.93 nm, which corresponds to the c and b cell parameters, respectively. The simulated image, using the structural model described above and calculated for a defocus value of $\Delta f = -30$ nm and a thickness of $t = 5$ nm, was found to be in good agreement with the experimental one and is shown as an inset in the right part of Fig. 4a (delimited with yellow asterisks). At this optimum defocus, the vanadium positions correspond to the dark dots and in the magnified area of the image displayed in Fig. 4b, the arrangement of the vanadium network perfectly fits with the dark blobs. A similar situation is found in the HRTEM image recorded along the $[010]$ zone axis (see Fig. 4c). In this case due to the presence of amorphous material in the surface of the nanobelts, a part of the image was filtered yielding a complex arrangement of dots, where we can detect a periodicity in contrast with values of 0.36 and 1.69 nm corresponding in this case to the parameters a and c of the orthorhombic unit cell (Fig. 4d). Note again the excellent matching between the calculated image delimited by yellow asterisks (defocus value of $\Delta f = -40$ nm and a thickness of $t = 6$ nm) and the experimental one

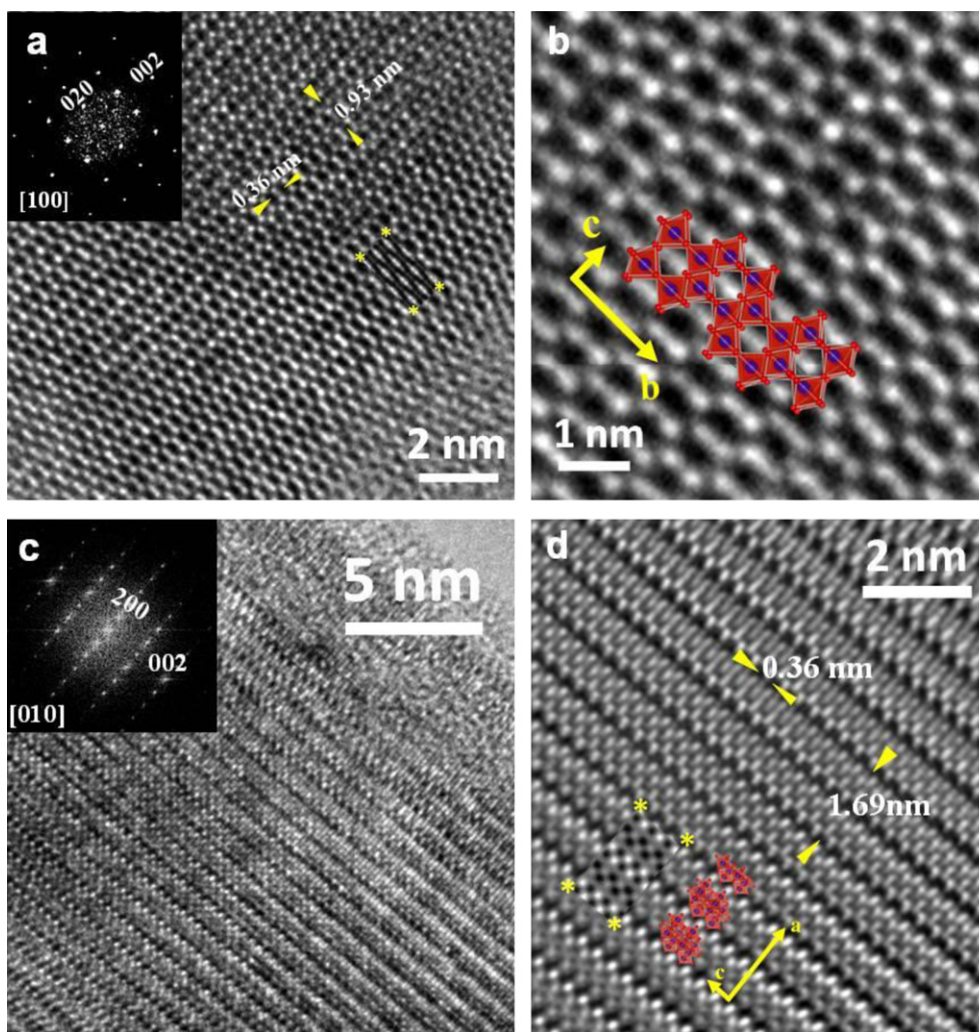
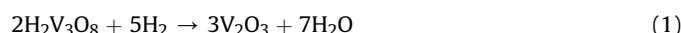


Fig. 4. a) HRTEM image of a $\text{H}_2\text{V}_3\text{O}_8$ crystal along the $[100]$ zone axis and its corresponding optical diffraction pattern; the calculated image is delimited by yellow asterisks; b) High magnification of (a) where the dark dots are clearly identified with the vanadium cations of the projected crystal structure; c) HRTEM image of the nanobelts along the $[010]$ zone axis and d) the corresponding filtered image showing the arrangement of the vanadium sheets (see the projected structure inserted) along the a axis and the excellent agreement with the calculated image delimited by yellow asterisks. (For interpretation of the references to color in this figure legend, the reader is referred to the web version of this article.)

(Fig. 4d). The dark dots of the image represent the arrangement in layers of the vanadium atoms along the a direction (see the projected model inserted in the image).

$\text{H}_2\text{V}_3\text{O}_8$ powder was analysed using TGA in a H_2/He atmosphere in order to determine if hydration water is present in the as prepared sample (Fig. 5). A very small weight loss (ca. 0.5%) below 100°C is observed and attributed to adsorbed species on the surface of the sample, such as ethanol and water, and an evident plateau appears corresponding to the stability range of pure $\text{H}_2\text{V}_3\text{O}_8$ sample. A second weight loss of 6.5% occurs around 200°C and is ascribed to the loss of water yielding V_3O_7 . Finally, as temperature increases under the reducing conditions another weight loss (13.5%) is observed around 500°C accounting for the reduction to V_2O_3 . Total weight loss between 75 and 500°C is 20.1%. This is the expected weight loss for the overall reaction (Eq. (1)):



The XRD analysis of the product obtained after heating at 500°C confirms the formation of V_2O_3 , in accordance with the above proposed equation. Taking these results into account, the presence of a significant amount of intercalated water or ethanol is discarded. Nevertheless, the as prepared $\text{H}_2\text{V}_3\text{O}_8$ has been dried below 100°C prior to the electrochemical characterisation to avoid the presence of absorbed substances.

Electrochemical properties of $\text{H}_2\text{V}_3\text{O}_8$ have been found to be highly dependent on the preparation method inasmuch as very different capacities have been reported. The early report by Legaigneur et al. [5] described the electrochemical behaviour of samples with low specific surface area ($2\text{--}3\text{ m}^2\text{ g}^{-1}$) that develop a capacity of 240 mAh g^{-1} in the $4\text{--}1.5\text{ V}$ voltage range. Their $\text{H}_2\text{V}_3\text{O}_8$ sample showed an increase of capacity upon cycling that was interpreted as due to the decrease of particle size by electrochemical grinding. Higher capacities ranging from 300 to 400 mAh g^{-1} and above have been afterwards reached in $\text{H}_2\text{V}_3\text{O}_8$ nanobelts with lengths larger than $10\text{ }\mu\text{m}$ and widths of several tens of nanometres [9,10,12,23]. Unfortunately, these reports do not give information on the specific surface area. Based on the results of Chine et al. [11], who prepared crystals of similar size and reported a specific surface area of $13\text{ m}^2\text{ g}^{-1}$, we assumed that a specific surface area of that order of magnitude is needed to enhance lithium insertion yielding high performances.

Specific surface area (SSA) of the sample herein investigated, produced by a green chemistry procedure, was measured by physisorption of nitrogen using the Brunauer, Emmett and Teller

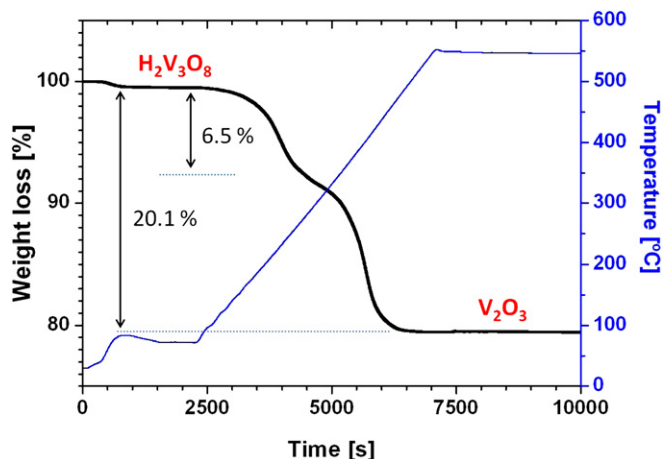


Fig. 5. Weight loss and temperature of a $\text{H}_2\text{V}_3\text{O}_8$ sample as a function of time under an atmosphere of H_2 (200 mbar)/ He (400 mbar). Heating rate: 5°C min^{-1} after 100°C .

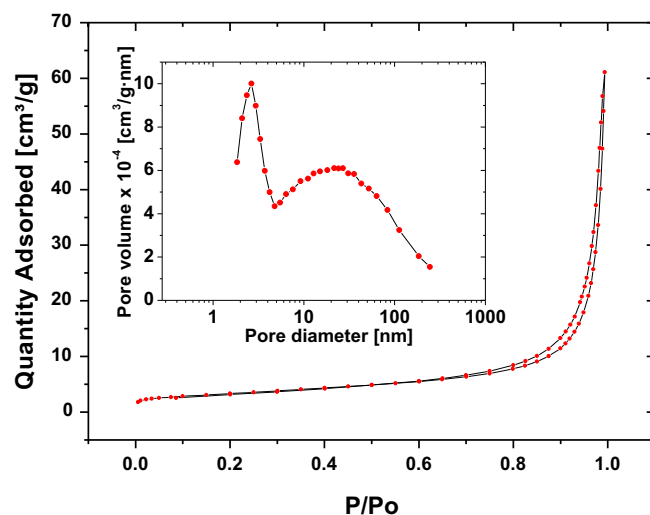


Fig. 6. N_2 adsorption–desorption isotherm of $\text{H}_2\text{V}_3\text{O}_8$ powder showing the amount of gas adsorbed versus the relative pressure. Inset: BJH pore size distribution derived from the adsorption branch of the isotherm.

(BET) method [20]. The N_2 adsorption–desorption isotherm of $\text{H}_2\text{V}_3\text{O}_8$ powder is presented in Fig. 6. The plot shows the amount of gas adsorbed ($\text{cm}^3\text{ g}^{-1}$) versus the relative pressure (P/P_o), where P is the equilibrium pressure of the adsorbed vapour and P_o is the saturated vapour pressure at the temperature of the experiment (77 K). This isotherm exhibits a hysteresis loop, where the lower branch represents measurements obtained by progressive addition of gas of the adsorbent, and the upper branch by progressive withdrawal. Such hysteresis is usually associated with the filling and emptying of meso-pores by capillary condensation. The isotherm is identified as type IV, typical of mesoporous materials [24]. The surface area determination using the BET technique yields a value of $11.92 \pm 0.02\text{ m}^2\text{ g}^{-1}$ for this material. Barrett–Joyner–Halenda (BJH) pore size distribution is shown in the inset of

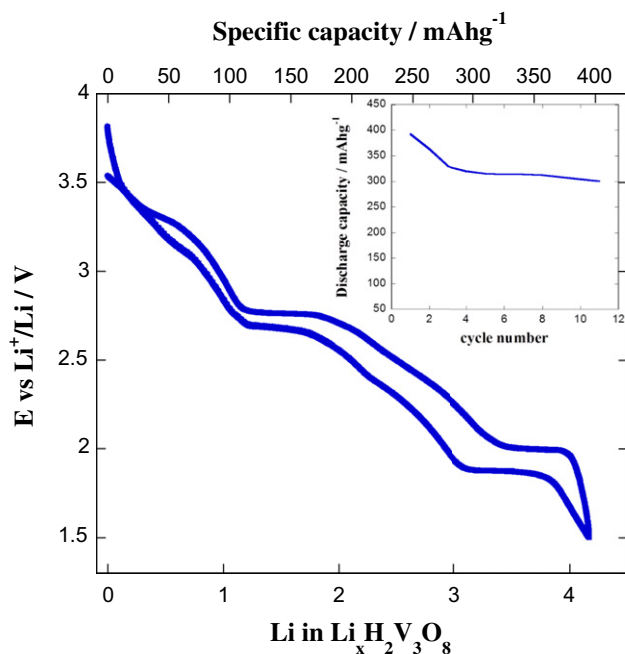


Fig. 7. Variation of voltage versus composition and corresponding specific capacity of $\text{H}_2\text{V}_3\text{O}_8$ discharged down to 1.5 V at a $C/20$ discharge rate. The inset shows the discharge capacity of the cell upon cycling.

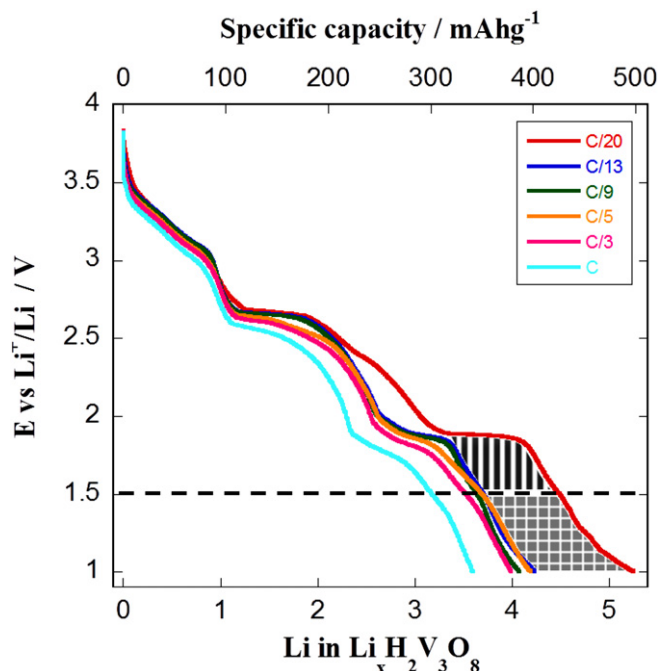


Fig. 8. Voltage variation versus composition and corresponding specific capacity of $\text{H}_2\text{V}_3\text{O}_8$ at different current rates (C/n). Note that n stands for the hours needed to insert 1 Li/f.u.

Fig. 6. From the distribution curve it is suggested a wide distribution of pores with small pore volume ($\approx 10^{-4} \text{ cm}^3 \text{ g}^{-1} \text{ nm}^{-1}$) and diameter mainly in the mesopore range (2–50 nm). It is possible to observe two peaks, the first narrow one corresponds to 2.6 nm pores, while the second peak shows a broad contribution with maxima about 24 nm pore size, probably due to the packing of the nanobelts.

Fig. 7 shows the typical electrochemical behaviour of $\text{H}_2\text{V}_3\text{O}_8$ nanobelts produced by the fast route herein described at C/20 ($\sim 4.7 \text{ mA g}^{-1}$) when the lower cut off voltage is set to 1.5 V. This is

the common value used in the very last studies reporting electrochemical performances of $\text{H}_2\text{V}_3\text{O}_8$ nanobelts produced by hydrothermal synthesis. A high capacity of 400 mA h g^{-1} is achieved. Hydrogen evolution, due to H^+ reduction upon lithium reaction, does not seem to take place in this case since discharge and charge curves have the same voltage profile even for deep discharges as it will be shown below (see Fig. 9a). This behaviour of $\text{H}_2\text{V}_3\text{O}_8$ is remarkable, because protonated systems tend to be unstable as it was observed recently for $\text{H}_2\text{Ti}_6\text{O}_{13}$ [25]. The absence of hydrogen displacement during lithium insertion in $\text{H}_2\text{V}_3\text{O}_8$ indicates that not all protonated systems must be discarded as prospective electrode materials. Nevertheless, a detailed structural determination of lithiated phases is being carried out to further clarify the role of hydrogen in the insertion reaction.

On the other hand, the cycling behaviour, shown in the inset of Fig. 7, reveals that a significant drop of capacity is observed after the first cycle though still a high capacity, ca. 300 mA h g^{-1} , is kept afterwards. Note that the loss of capacity after the first cycle seems to be a characteristic of $\text{H}_2\text{V}_3\text{O}_8$ nanobelts when cycled in the 4–1.5 V, range as deduced from previously reported data [9,10,12]. In order to shed some light on this capacity loss, the solubility of $\text{H}_2\text{V}_3\text{O}_8$ in the electrolyte and the structural stability of $\text{H}_2\text{V}_3\text{O}_8$ were investigated.

Vanadium content of the electrolyte was analysed by ICP in both cells cycled 5 times and in the solution obtained after stirring $\text{H}_2\text{V}_3\text{O}_8$ with the electrolyte for 24 h. In both cases only very small amounts ($1.6 \pm 0.2 \text{ ppm}$ and $10.4 \pm 0.5 \text{ ppm}$, respectively) of vanadium were detected. On the other hand, the X-ray diffraction pattern of the electrode after a discharge down to 1.5 V showed that main reflections of $\text{H}_2\text{V}_3\text{O}_8$ are maintained as expected for a topotactic reaction. However, some intensity changes and peak shifts were detected. A more detailed study of these changes will require the combination of neutron diffraction and X-ray diffraction using synchrotron radiation to determine the structure of lithiated phases as above mentioned. Results will be reported elsewhere.

Therefore, we conclude that the capacity loss after the first cycle is likely more related to processing or morphology issues of the electrode than to the reversibility of insertion reaction or dissolution of active material.

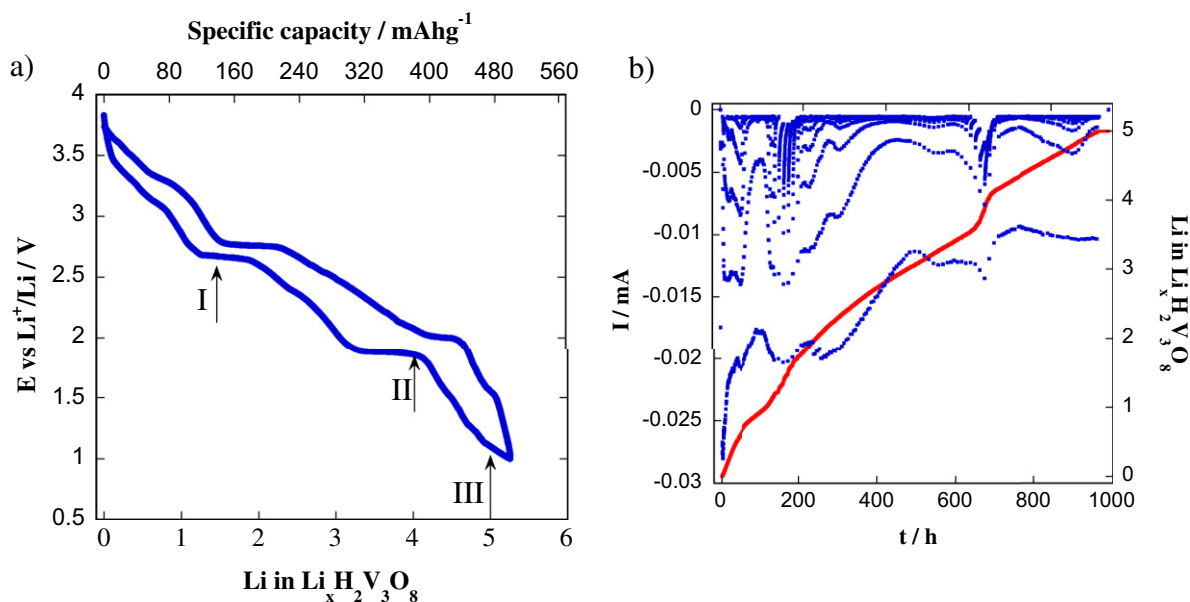


Fig. 9. a) Variation of voltage versus composition and corresponding specific capacity of $\text{H}_2\text{V}_3\text{O}_8$ discharged down to 1 V at a C/20 discharge rate and b) PITT quasi-equilibrium measurement on a $\text{Li}/\text{H}_2\text{V}_3\text{O}_8$ cell at $\pm 10 \text{ mV}$ for 12 h down to 1.0 V.

The discharge behaviour of $\text{H}_2\text{V}_3\text{O}_8$ at different current rates varying from C/20 to 1C and down to 1 V is shown in Fig. 8. The horizontal line indicates the lower cut off voltage that has been normally used when researching this material (1.5 V). Up to date, the highest capacity reported for $\text{H}_2\text{V}_3\text{O}_8$, 409 mAh g⁻¹, corresponds to the insertion of 4.32 Li/f.u. at a current rate of 20 mA g⁻¹ [9]. Although a simple comparison with data depicted in Fig. 8 is difficult due to differences in electrode processing and fabrication (type of current collector, electrode surface, nature and quantity of carbon black, binder, etc.), it can be seen that the herein presented capacity data in the 3.75–1.5 V range (limited by the horizontal dashed line in Fig. 8) vary from 4.48 Li/f.u. (425 mAh g⁻¹) for C/20 (4.7 mA g⁻¹) to 3.2 Li/f.u. (300 mAh g⁻¹) for 1C (87 mA g⁻¹). Therefore, it can be concluded that quite good electrochemical performances are reached for the sample prepared following the proposed fast, cost-effective and green chemistry procedure and being comparable to those obtained for $\text{H}_2\text{V}_3\text{O}_8$ prepared by less cost-effective and green procedure [9,10,12,23]. Fig. 8 also shows that polarisation increase at high current rate seems to become more significant beyond intercalation of 2 Li/f.u. (see shaded areas in Fig. 8) likely due to a slower Li diffusion and more severe structural stress.

As it was shown in Fig. 7, the discharge down to 1.5 V corresponds to the insertion of ca. 4.2 Li/f.u. Thus at this voltage a mixed $\text{V}^{4+/3+}$ state is expected. In order to test if $\text{H}_2\text{V}_3\text{O}_8$ inserts more lithium in a reversible way, some cells were discharged to a lower voltage and charged back to 3.75 V. A full discharge–charge cycle in the 3.75–1.0 V voltage range of a lithium cell bearing our $\text{H}_2\text{V}_3\text{O}_8$ material as the positive electrode material is presented in Fig. 9a. The cycling experiment in the 3.75–1.0 V range shows for the first time the reversible insertion of a lithium quantity that corresponds to the complete reduction of 2 V^{5+} and 1 V^{4+} to 3 V^{3+} , this is 5 Li/f.u.

Therefore, the reversible insertion of 5 Li/f.u. unveils that this material develops a very large reversible capacity of ca. 498 mAh g⁻¹ which is much higher than previously reported values [9,10,12,23], because it allows a deeper discharge. However, from data shown in Fig. 8 note that the extra capacity obtained at low voltage (below 1.8 V) is very sensitive to current rate, since as soon as current rate increases from C/20 to C/13 a large drop of energy occurs but involving mainly the energy developed at low voltage, below 1.8 V (see shaded area below 1.5 V in Fig. 8). Then for practical use we may consider only the capacity obtained down to 1.5 V, in the order of 400 mAh g⁻¹.

Interestingly, the features of the voltage–composition profile are clearly seen in Fig. 9a allowing the identification of the solid solution and two-phase regions (continuous variation and plateaus of voltage, respectively). The nature of the mentioned regions is more clearly seen in Fig. 9b, where the relaxation of current with time during a potentiostatic discharge is shown in the whole intercalation range. Thus it can be seen that for reaction time t ca. 175 h and 675 h, current relaxation follows an anomalous behaviour far from a $t^{-1/2}$ law indicating that lithium diffusion is not ruling the intercalation reaction. Those two regions are then assigned to biphasic regions. In the rest of regions the expected relaxation trend indicates that a single phase of variable composition is being formed. However, in spite of the long time the system was allowed to relax, a limited kinetics is observed throughout the whole intercalation regions, inasmuch as current does not relax to zero. As expected the effect of limited kinetics is more evident in the two-phase regions, where lithium diffusion through the interphase shows a delayed reaction. A complete investigation of the structure of the $\text{Li}_x\text{H}_2\text{V}_3\text{O}_8$ phases including the variation of lithium diffusion coefficient will be reported elsewhere.

In order to know the changes in vanadium oxidation state we have isolated several samples in the $0 \leq x \leq 5$ compositional

range by discharging different cells down to 2.65, 1.85 and 1.0 V. The corresponding compositions $\text{Li}_x\text{H}_2\text{V}_3\text{O}_8$ ($x = 1.5, 4.0$ and 5.0), located on the discharge–charge curve shown in Fig. 9 as I, II and III, were further characterised by EELS. Of particular interest is the last one, since it represents the maximum lithium quantity that $\text{H}_2\text{V}_3\text{O}_8$ can insert reversibly.

It is well known that the white lines in the 3d transition metals are sensitive to valence changes and the position and total intensity or L_3/L_2 ratio of these lines can be used to extract this information [26]. Another method that was shown to give good results is to measure the difference in energy onset between the oxygen K edge and the transition metal L_{23} edge of oxides [27]. In the case herein

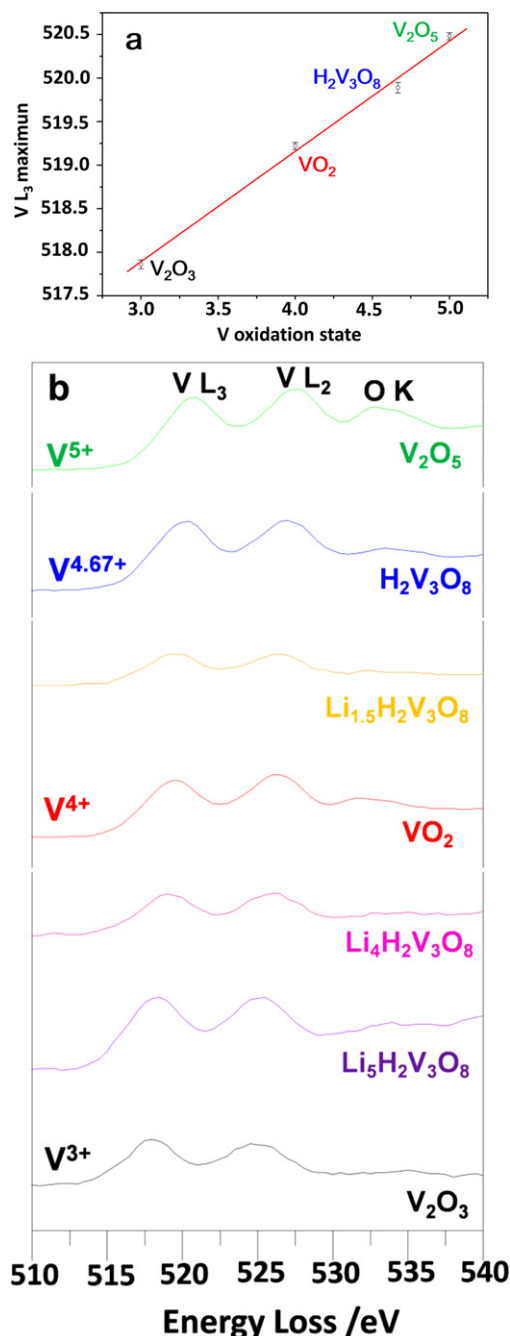


Fig. 10. a) Graph showing the linear increase of the V L_3 maximum position with vanadium oxidation state (R factor of 0.993); b) ELNES of vanadium L_{23} edges from the oxides used in the calibration and the lithiated materials $\text{Li}_x\text{H}_2\text{V}_3\text{O}_8$ with $x = 1.5, 4.0$ and 5.0 , sorted by their oxidation state.

investigated since the V L_{23} edge and the O K edge overlap, we adopted a modification of the last method and in our approximation we compare the shift of the V L_{23} for different reference compounds, the pristine $H_2V_3O_8$ nanobelts and the Li intercalated materials with respect to the C K edge used as reference for energy calibration. Note that latter materials are mixed with carbon black due to the preparation route (see details in the experimental section). According to this, V_2O_3 (V^{3+}), VO_2 (V^{4+}), $H_2V_3O_8$ ($V^{4.67+}$) and V_2O_5 (V^{5+}) samples mixed with carbon were used as valence standard. Linear fitting of the vanadium L_3 energy maximum (E_{L3}) and the vanadium oxidation state (V_V) shows a relation following $E_{L3} = a + b V_V$ with $a = 514.05(27)$ and $b = 1.27(6)$ (Fig. 10a).

If we represent now the V L_{23} edge of $Li_xH_2V_3O_8$ with $x = 0, 1.5, 4.0$ and 5.0 , together with the reference compounds (Fig. 10b), it can be observed that for low lithium content the V L_3 edge is close to those of V_2O_5 and VO_2 . However, it shifts towards VO_2 and V_2O_3 for higher lithium content and finally is similar to that of V_2O_3 for $x = 5.0$. The average oxidation state of vanadium for $Li_xH_2V_3O_8$ with $x = 1.5, 4.0$ and 5.0 can be estimated from the linear relationship plotted in Fig. 10a as being $+4.10(16)$, $+3.80(15)$ and $+3.10(12)$. These results fairly agree with the expected variation of average oxidation state ($+4.2, +3.4, +3.0$) accordingly to their composition. Interestingly, full reduction to V^{3+} is confirmed for the first time in this electrode material.

4. Conclusions

A new synthesis procedure combining hydrothermal and microwave techniques is presented to obtain the electrode material $H_2V_3O_8$ with nanobelt morphology of about 100 nm wide and several micrometres long. Compared to previously reported hydrothermal procedures, the herein presented route is faster, less expensive and more environmentally friendly. Only V_2O_5 , water and ethanol are used to prepare the electrode material in just 2 h. The characterisation performed confirmed the production of $H_2V_3O_8$ with the adequate morphology to exhibit high electrochemical performances. At C/20 an initial capacity of ca. 400 mAh g^{-1} is developed in the 3.75–1.5 V range. After a significant capacity loss in the first cycle, a capacity of ca. 300 mAh g^{-1} is maintained upon cycling. Full reduction to V^{3+} has been observed for the first time by discharging Li cells with $H_2V_3O_8$ as the cathode down to 1 V; a significant increase of reversible capacity to 498 mAh g^{-1} is thereby obtained. However, this extra capacity is more readily lost at high current rate than capacity developed above 2 V. Then for practical use we may consider only the capacity obtained down to 1.5 V. Furthermore, the similarity of discharge and charge curves, pointing to the absence of hydrogen displacement during lithium insertion in $H_2V_3O_8$ indicates that not all protonated systems must be necessarily discarded as prospective electrode materials.

Acknowledgements

We thank Ministerio de Economía y Competitividad and Comunidad de Madrid for funding the projects MAT2010-19837-C06 and S2009/PPQ-1626 respectively. Financial support from Universidad CEU San Pablo is also acknowledged. Prof. María José Torralvo (UCM) is gratefully acknowledged for her contribution to the surface and textural analysis.

References

- [1] T. Chirayil, P.Y. Zavalij, M.S. Whittingham, *Chemistry of Materials* 10 (1998) 2629–2640.
- [2] K.-H. Chang, C.-C. Hu, *Acta Materialia* 55 (2007) 6192–6197.
- [3] M. Niederberger, H.J. Muhr, F. Krumeich, F. Bieri, D. Gunther, R. Nesper, *Chemistry of Materials* 12 (2000) 1995–2000.
- [4] V. Luca, J.M. Hook, *Chemistry of Materials* 9 (1997) 2731–2744.
- [5] V. Legagneur, A.L. La Salle, A. Verbaere, Y. Piffard, D. Guyomard, *Electrochimica Acta* 47 (2002) 1153–1161.
- [6] V. Legagneur, A.L. La Salle, A. Verbaere, Y. Piffard, D. Guyomard, *Journal of Materials Chemistry* 10 (2000) 2805–2810.
- [7] F. Theobald, R. Cabala, *Comptes Rendus Hebdomadaires Des Seances De L Academie Des Sciences Serie C* 270 (1970) 2138.
- [8] Y. Oka, T. Yao, N. Yamamoto, *Journal of Solid State Chemistry* 89 (1990) 372–377.
- [9] S. Gao, Z. Chen, M. Wei, K. Wei, H. Zhou, *Electrochimica Acta* 54 (2009) 1115–1118.
- [10] S. Mho, C.V. Reddy, Y. Kim, I. Yeo, S. Park, *Journal of Korean Physical Society* 54 (2009) 2420–2424.
- [11] M.K. Chine, F. Sediri, N. Gharbi, *Materials Sciences and Applications* 2 (2011) 964–970.
- [12] Y. Zhang, X. Liu, G. Xie, L. Yu, S. Yi, M. Hu, C. Huang, *Materials Science and Engineering B-Advanced Functional Solid-State Materials* 175 (2010) 164–171.
- [13] S. Komarneni, R. Roy, Q.H. Li, *Materials Research Bulletin* 27 (1992) 1393–1405.
- [14] J. Prado-Gonjal, R. Schmidt, J. Espíndola-Canuto, P. Ramos-Alvarez, E. Morán, *Journal of Power Sources* 209 (2012) 163–171.
- [15] B.L. Hayes, *Microwave Synthesis: Chemistry at the Speed of Light*, CEM Publishing, Matthews, NC, 2002.
- [16] H.M. Kingston, S.J. Haswell, *Microwave-Enhanced Chemistry*, American Chemical Society, 1997.
- [17] J.-M. Li, K.-H. Chang, T.-H. Wu, C.-C. HU, *Journal of Power Sources* (2012). <http://dx.doi.org/10.1016/j.jpowsour.2012.09.007>.
- [18] J. Prado-Gonjal, D. Ávila, M.E. Villafuerte-Castrejón, F. González-García, L. Fuentes, R.W. Gómez, J.L. Pérez-Mazariego, V. Marquina, E. Morán, *Solid State Sciences* 13 (2011) 2030–2036.
- [19] J. Rodríguez Carvajal, *Physica B* 192 (1993) 55–69.
- [20] S. Brunauer, P.H. Emmett, E. Teller, *Journal of the American Chemical Society* 60 (1938) 309–319.
- [21] B. Davis, *The Journal of Physical Chemistry* 90 (1986) 4701–4705.
- [22] Y.-S. Bae, A.O.Z.R. Yazaydin, R.Q. Snurr, *Langmuir* 26 (2010) 5475–5483.
- [23] H. Li, T. Zhai, P. He, Y. Wang, E. Hosono, H. Zhou, *Journal of Materials Chemistry* 21 (2011) 1780–1787.
- [24] F. Rouquerol, J. Rouquerol, K. Sing, *Adsorption by Powders and Porous Solids*, Academic Press, France, 1999.
- [25] J.C. Perez-Flores, C. Baetz, M. Hoelzel, A. Kuhn, F. Garcia-Alvarado, *RSC Advances* 2 (2012) 3530–3540.
- [26] H.K. Schmid, W. Mader, *Micron* 37 (2006) 426–432.
- [27] D. Bach, H. Stoermer, R. Schneider, D. Gerthsen, J. Verbeeck, *Microscopy and Microanalysis* 12 (2006) 416–423.